Title

Modeling singular mineralization processes due to fluid pressure fluctuations

Authors

Xiong, Y
Zuo, R
Clarke, KC
et al.

Publication Date

2020-03-05

DOI

10.1016/j.chemgeo.2019.119458

Peer reviewed

Modeling singular mineralization processes due to fluid pressure fluctuations

Yihui Xiong[1,2], Renguang Zuo[1,*], Keith C. Clarke[2], Stephen A. Miller[3], Jian Wang[4]

[1]State Key Laboratory of Geological Processes and Mineral Resources, China University of Geosciences, Wuhan 430074, China

[2]Department of Geography, University of California, Santa Barbara, CA, USA 93106-4060

[3]Center for Hydrogeology and Geothermics, University of Neuchatel, rue Emile Argand 11, Neuchâtel, Switzerland

[4]Key Laboratory of Geoscience Spatial Information Technology of Ministry of Land and Resources, Chengdu University of Technology, Chengdu, 610059, Sichuan, China

*Corresponding Author. Email: zrguang@cug.edu.cn

Abstract

Mineralization in the Earth's crust can be regarded as a singular process resulting in large amounts of mass accumulation and element enrichment over short time or space scales. The elemental concentrations modeled by fractals and multifractals show self-similarity and scale-invariant properties. We take the view that fluid-pressure variations in response to earthquakes or fault rupture are primarily responsible for changes in solubility and trigger transient physical and chemical variations in ore-forming fluids that enhance the mineralization process. Based on this general concept, we investigated mineral precipitation processes driven by rapid fluid pressure reductions by coupling mineralization to a cellular automaton model to reveal the nonlinear mechanism of the orogenic gold mineralization process using simulation. In the model, fluid pressure can increase to the rock failure condition, which was set as lithostatic pressure at a depth of 10km (270MPa), due to either porosity reduction or dehydration reactions. Rapid drops in pressure resulting from fault rupture or local hydrofracture may induce repeated gold precipitation. The geochemical patterns generated by the model evolve from depletion to enrichment patterns, and from

spatially random to spatially clustered structures quantified by multifractal models and geostatistics. Results show how metal elements self-organize to form high metal concentration patterns displaying self-similarity and scale-invariance. These transitions are attributed to the growth and coalescence of sub-networks with different fluid pressures up to the percolation threshold, resulting in a wide range of fluid pressure reductions and mineral precipitation in the form of clusters. The results suggest that cyclic evolution of fluid pressure and its effects on gold precipitation systems can effectively mimic the repeated mineralization superposition process, and generate complex geochemical patterns characterized by a multifractal model. The nonlinear behavior exhibits scale-invariance and self-organized critical threshold,s where mineral phase separations result from fluid pressure reductions associated with fault failure.

Keywords: Singular mineralization process; Fluid pressure fluctuation; Cellular automaton; Self-organized criticality

1. Introduction

The interactions of fluid flow, seismicity, and mineral precipitation can control the mechanical strength and permeability of faults in the earth's crust, and are indispensable components in the development of hydrothermal systems and the formation of ore deposits (Sibson, 1987; Sibson et al., 1988; Cox, 1995; Weatherley and Henley, 2013). Mechanisms responsible for generation and maintenance of high fluid pressure are closely related to the spatial (Rice, 1992) and temporal (Walder and Nur, 1984) variations of local permeability. In seismic zones, fluid pressure increases within impermeable zones and occurs from creep compaction (Sprunt and Nur, 1977), pressure solution (Sleep and Blanpied, 1992), fracture healing and sealing (Walder and Nur, 1984; Sibson et al., 1988; Blanpied et al., 1992). In addition, direct fluid sources involving fluids at depth or from devolatilization reactions have also been considered as mechanisms for elevated fluid pressure (Rice, 1992; Ko et al., 1995; Miller et al., 2003; Bodnar et al.,

2007). Once the fluid pressure increases to a level sufficient to permit frictional slip at low fault shear stress, permeability instantaneously increases by several orders of magnitude to locally extremely high values (Miller and Nur, 2000). The rapid fluid pressure reductions due to fault ruptures can induce boiling, or phase separation of ore fluids contributing to mineral deposition (Sibson, 1987; Sibson et al., 1988; Wilkinson and Johnston, 1996; Weatherley and Henley, 2013; Peterson and Mavrogenes, 2014). Rapid deposition during a fluid pressure decrease seals fractures, returning permeability again to a very low value, and the cycle repeats (Sibson et al., 1988; Sibson, 1992).

This well-known fault-valve process is widely linked to the formation of mesothermal gold mineralization because the rapid fluid pressure reductions due to fault ruptures can result in anomalous enrichment of elements in small ore bodies within a relatively short period of time (Sibson et al., 1988; Wilkinson and Johnston, 1996; Weatherley and Henley, 2013; Peterson and Mavrogenes, 2014; Sanchez-Alfaro et al., 2016; Moncada et al., 2019). This process is in accordance with the singular mineralization process, which can result in anomalous amounts of mass accumulation and element enrichment within a narrow spatio–temporal interval (Cheng, 2007, 2008; Zuo et al., 2009). The end products of the singular mineralization processes often show complex non-linear properties, and can be modeled by fractals and multifractals (Cheng et al., 1994; Cheng and Agterberg, 1996; Agterberg, 1995; Cheng et al., 2000; Cheng, 2007, 2008; Zuo et al., 2009; Zuo and Wang, 2016; Zuo, 2016, 2018).

The concept of fractals introduced by Mandelbrot (1983) primarily represents irregular geometry by its Hausdorff (or fractal) dimension, which is greater than its topological dimension. Multifractals are spatially intertwined fractals with a continuous spectrum of fractal dimensions, which can be used for describing complexity and self-similarity in nature. Examples include the spatial distribution of geological and geochemical quantities, such as mineralization-related element concentrations in rock or related surface media, such as water, soils, and stream sediments (Cheng et al., 1994; Cheng and Agterberg, 1996; Cheng, 1999; Cheng, 2007). Both deterministic and stochastic physical models, such as self-organized

criticality, multiplicative cascade processes, diffusion limited aggregation, turbulence and Brownian motion (Bak et al., 1987; Schertzer and Lovejoy, 1987; Evertsz and Mandelbrot, 1992) illustrate the generation of fractals or multifractals. For example, the theory and concept of multiplicative cascade processes play an important role describing intermittent turbulence and nonlinear processes (Schertzer and Lovejoy, 1987). The de Wijs model (De Wijs, 1951; Agterberg, 2001) is a simple multiplicative cascade model widely applied for explaining the generation mechanism of multifractal patterns and their basic singularity characteristics in regional exploration geochemistry (Agterberg, 2001, 2007; Cheng, 2005; Xie and Bao, 2004). However, they cannot efficiently reflect the effects of the variations in extreme physical processes (e.g. fluid pressure fluctuation) on the evolution of the hydrothermal systems. As a numerical equivalent of the fault valve model, the coupled cellular automaton with shear stress and fluid pressure proposed by Miller et al. (1996, 1999) is expected to simulate the singular mineralization process from fluid pressure fluctuation. In this model, fluid flow within a fault zone is modeled as a simple cellular automaton model with a 'toggle switch' permeability assumption (Miller and Nur, 2000). That is, permeability is set to two extreme states, either zero when the fluid pressure fails to reach the failure conditions along the fault plane, or infinite to the nearest neighbors when the fluid pressure reaches the condition, and a dilatant slip event occurs (Miller and Nur, 2000). The dynamical system between shear stress and the state of the fluid pressure exhibits an evolution to a complex stress state that results in scale-invariant and self-organizing behavior (Miller et al., 1996, 1999; Miller and Nur, 2000; Fitzenz and Miller, 2001; Miller, 2002; Miller et al., 2003).

However, these models focused on the dynamic interaction between earthquakes and dehydration reactions, and did not address mineral precipitation processes associated with rapid fluid pressure reductions. Gold solubility in hydrothermal solutions is dominantly controlled by temperature, pressure, pH, and redox (e.g., Seward, 1973). A drop in pressure alone initiates gold precipitation (Loucks and Mavrogenes, 1999), yet decompression also triggers phase separation where the exsolution of volatiles

drastically alters fluid chemistry to induce precipitation. Recent studies have suggested that precious metal solubilities are strongly dependent on water vapor phase as the density of the fluid changes, which is an indirect measure of changing fluid pressure (Migdisov and Williams-Jones, 2013). The abrupt reductions in fluid pressure may have a dramatic effect on the aqueous solubility of quartz (Walther and Helgeson, 1977) and are likely to play a major role in co-precipitation of gold with silica during each fault rupture (Helgeson and Lichtner, 1987; Migdisov and Williams-Jones, 2013; Weatherley and Henley, 2013).

In this study, we integrated the mineral precipitation process into the fluid flow cellular automaton to investigate the basic nonlinear behaviors of the orogenic gold mineralization process during rapid fluid reductions due to fault failure at a depth of 10km (270MPa). We coupled gold precipitation processes to the model of Miller and Nur (2000) to investigate how metal elements self-organize to form ore deposits with high metal concentrations showing self-similarity. The complexity and self-similarity of generated metal concentrations was further quantified by a multifractal model and geostatistics (Matheron, 1962; Goovaerts, 1999).

2. Models

2.1 Numerical model

Cellular automata can generate very complex forms according to a simple set of local rules governing interactions among nearest neighbors, and thus are attractive for the study of critical phenomena and phase transitions (Wolfram, 1984; Bak et al., 1987; Bak and Tang, 1989; Miller et al., 1996). We assume a grid of cells at depth representing a cross section through an active fault zone. The state of each cell within a fault plane is determined by fluid pressure P_f, which is in hydraulic isolation from its neighbors until a failure condition is reached. When the fluid pressure is sufficient to induce hydro-fracture or other failure mechanism such as frictional sliding, the permeability is assumed infinite to the nearest neighboring cells and fluid pressure equilibrates with neighboring cells by conserving fluid mass.

The fluid pressure in each cell within the impermeable fault zone is increased at a uniform driving rate at each time-step (t):

$$P_f \rightarrow P_f + \frac{\partial P_f}{\partial t}|_{noflow}, \frac{\partial P_f}{\partial t}|_{noflow} = \frac{(\dot{\Gamma} - \dot{\phi})_i}{\phi_i(\beta_\phi + \beta_f)_i} \quad \text{(Eq. 1)}$$

where $\dot{\Gamma} - \dot{\phi}$ represents the fluid pressure source coupled with a time dependent porosity reduction ($-\dot{\phi}$) and a direct fluid source ($\dot{\Gamma}$), ϕ_i represents the initial porosity in cell *i*; and β_ϕ and β_f represent the pore and fluid compressibility, respectively, often lumped into a single parameter $\beta = \beta_\phi + \beta_f$ (Segall and Rice, 1995; Wong et al., 1997). Porosity reduction mechanisms (e.g., fault compaction and pressure solution) and a direct fluid source (e.g., dehydration/decarburization reactions) contribute to the increases of fluid pressure acting on discrete cells of a zero permeability fault plane. Once fluid pressure exceeds the lithostatic load, failure occurs, and the failed cells and their immediate neighboring cells are labeled. The fluid pressure instantaneously equilibrates with these hydraulically connected cells by conserving fluid mass, ignoring any gravity effect. The equilibrium fluid pressure within the affected cells updates to:

$$\overline{P} = \frac{\sum_{i=1}^{N}(\phi\beta)_i P_i}{\sum_{i=1}^{N}(\phi\beta)_i} \quad \text{(Eq. 2)}$$

where P_i and $\overline{P}$ represent the pre-failure and post-failure pore pressure among the affected cells, respectively, and N is the number of affected cells. The fluid pressure redistribution might cause the neighboring cells to reach the failure condition, leading to further pressure equilibrium and cascading failure until the stress value in all the cells recovers to below the failure condition. It is important to note that the numerous mechanisms (e.g., crack porosity production due to hydro-fracture, variation of mechanical strength, and time-dependent healing), that are responsible for the evolution of fluid pressure, are simplified in this model (Miller and Nur, 2000).

Once the fault rupture occurs, the abrupt drop in fluid pressure toward hydrostatic values triggers mineral precipitation in the fracture network, which can seal fractures to rebuild the fluid pressure and ensure that the cycle repeats. The relationship between the solubility of elements and fluid pressure is different for different temperature ranges. Some studies suggest that the solubility of metal ion species (e.g. Ag, Au, Cu and Sn) decreases log-linearly with decreasing water vapor pressure (Migdisov et al., 1999; Archibald et al., 2001, 2002; Migdisov and Williams-Jones, 2005). Other studies show an exponential relationship between metal ions and water vapor pressure with the change of temperature (Bischoff et al., 1986, 1988; Rempel et al., 2006; Migdisov and Williams-Jones, 2013; Migdisov et al., 2014). These studies indirectly reflect that the fluid pressure can efficiently affect the solubility of precious metal solubilities.

We recognize that fluid pressure is not the only factor that controls metal solubility in hydrothermal systems, and other physical and chemical factors, such as temperature, pH and redox, may be as important or more important in some cases (Seward, 1973). Here, we ignore these other factors for the sake of simplicity and focus only on the role of pressure decrease as the mechanism of metal deposition.However, if the hydrothermal fluid is still undersaturated after the solubility decreases due to an abrupt pressure drop, the metal will not precipitate. Thus, to simplify the model, we suppose that each solubility decrease can lead to metal precipitation because the subsequent recovery stage flow of fluid from the surroundings into the sealing factures can progressively build high concentration hydrothermal fluid cycle by cycle (Weatherley and Henley, 2013).

In this study, we used three different relationships between metal ions and fluid pressure. Specifically, we investigate linear, exponential and power-law functions (Eq. 3) to estimate the volume of mineral precipitation.

$$\begin{cases} Linear: \log S_{metal} = A + B \cdot \log P_f \\ Power: \log S_{metal} = A + B \cdot (\log P_f)^C \\ Exponential: \log S_{metal} = A + B \cdot C^{\log P_f} \end{cases} \quad \text{(Eq. 3)}$$

Taking the linear relationship as an example, the volume of mineral precipitation due to rapid fluid pressure reductions can be estimated by:

$$C_{metal} = \left(S_{metal} - \overline{S}_{metal}\right) \cdot \phi\beta = 10^{A} \cdot \left(P_f^B - \overline{P}_f^B\right) \cdot \phi\beta \quad \text{(Eq. 4)}$$

Here C_{metal} represents the mineral element concentration in the cells. S_{metal} and $\overline{S}_{metal}$ represent the solubility of metals corresponding to pre-failure fluid pressure P_f and post-failure fluid pressure $\overline{P}_f$, respectively, and *A*, *B* and *C* are constants. The cell storage capacity ($\phi\beta$) is considered as the fluid mass of each cell.

2.2 Multifractal model and singularity

We assume that the total concentration of deposited metal elements (e.g., Au or Ag) in the *i*-th cell with a linear measuring scale ε satisfies $\mu_i(\varepsilon) \propto \varepsilon^{\alpha_i}$ from a multifractal perspective, where α_i represents the singularity index. Different cells possess different singularity indices, hence the total number of cells covering the entire subset bearing the singularity α, $N_\alpha(\varepsilon)$, is proportional to $\varepsilon^{-f(\alpha)}$ ($N_\alpha(\varepsilon) \propto \varepsilon^{-f(\alpha)}$). The fractal dimension function $f(\alpha)$ is known as a multifractal spectrum, which is usually estimated via the moment method (Halsey et al., 1986). The partition function $\chi_q(\varepsilon)$ is defined as:

$$\chi_q(\varepsilon) = \sum_{N(\varepsilon)} \mu_i^{\,q}(\varepsilon) \quad \text{(Eq. 5)}$$

The partition function $\chi_q(\varepsilon)$ shows a power-law relationship with cell size ε for any $q \in [-\infty, +\infty]$ if the distribution of $\mu_i(\varepsilon)$ is multifractal,

$$\chi_q(\varepsilon) \propto \varepsilon^{\tau(q)} \quad \text{(Eq. 6)}$$

Here $\tau(q)$ represents the mass exponent of order *q*. The index $M = \tau(2) - 2\tau(1) + \tau(0) < 0$ suggests that the measure corresponds to a multifractal, whereas M=0 suggests a fractal or non-fractal.

The singularity exponent $\alpha(q)$ and the multifractal spectrum value can be calculated through the mass exponent by differentiation and the Legendre transformation, respectively (Evertsz and Mandelbrot, 1992)

185 $$\alpha(q) = \frac{d\tau(q)}{q}$$ (Eq. 7)

186 $$f[\alpha(q)] = \alpha(q)q - \tau(q)$$ (Eq. 8)

187 An asymmetry index $R = (\alpha(0) - \alpha_{\min})/(\alpha_{\max} - \alpha(0))$ is defined to quantify the shape of the entire
188 multifractal spectrum (Xie and Bao, 2004; Cheng, 2014). R > 1 or R < 1 represent a left- or right-skewed
189 shape of the multifractal spectrum indicating that a local enrichment or depletion pattern dominates
190 among the whole set of cells, respectively.

191

192 2.3 Semivariogram

193 Semivariograms are a key component in geostatistics, and are typically used to quantify the degree
194 of spatial variability. The semivariogram function can be expressed as:

195 $$\gamma(h) = \frac{1}{2N(h)} \sum_{i=1}^{N(h)} [Z(x_i) - Z(x_i + h)]^2$$ (Eq. 9)

196 where $\gamma(h)$ represents the semivariance that quantifies the average dissimilarity between the measured
197 variable at different spatial locations. $Z(x_i)$ and $Z(x_i + h)$ represent the value of a variable at locations *i*
198 and *i* + *h*, respectively, and *N(h)* is the number of data pairs separated by a given lag vector *h*. The basic
199 concepts involved in the semivariogram include a measure of the total variance (the sill, C_0 + C), the
200 average length of the spatial dependence (range), and the local variation due to sampling or measurement
201 error (the nugget, C_0). The degree of spatial dependence is determined by the ratio of the nugget to sill: C_0 /
202 C_0+C < 0.25 (strong spatial dependence), 0.25 < C_0 / C_0+C < 0.75 (moderate spatial dependence) and C_0 /
203 C_0+C > 0.75 (weak spatial dependence) (Cambardella et al., 1994).

204

205

206 **3. Results**

We started the simulation of fluid pressure increases and mineral precipitation process within a test grid of $L \times L$ ($L = 200$) cells. Different distributions of fluid sources and material properties (simplified to initial porosity and the compressibility of pore space and fluid) may determine the distribution of the fluid pressure rate of increase (Miller and Nur, 2000). In our study, we considered a heterogeneous fault zone where the initial value of compressibility varies, and the source term remain constant. The compressibility was set between 1×10^{-3} MPa^{-1} and $1\times10^{-2}MPa^{-1}$ based on experimental results from David et al. (1994). The storage capacity was varied from 5×10^{-5} MPa^{-1} to 5×10^{-4} MPa^{-1} by setting the initial porosity to 0.05. The source term was set to a constant value of 1×10^{-6} yr^{-1}. The initial fluid pressure in each cell was distributed between the hydrostatic and lithostatic pressures, in which lithostatic pressure was regarded as the failure condition, and set to 270MPa corresponding to a depth of 10km. These parameters result in fluid pressure increasing towards the failure condition at rates ranging from 2-20 kPa/yr. At early simulation times, cells reaching failure are independent in space because the neighbors of the failed cells are far from failure, thus preventing the propagation of the failure event and limiting the event size. We define event size as the total number of cells reaching the failure condition during one discrete time-step. As the simulation evolves, many cells approach the failure condition, and the high pressure in the failed cells can propagate quickly to generate large events. Once failure occurs during the simulation, the fluid pressure in an individual cell or cluster of cells experiences abrupt fluctuations from hydraulic connectivity to low pressure cells. The abrupt fluid pressure drops reduce the solubility of precious metals (e.g. Ag and Au), which is likely to induce co-precipitation of gold with silica during each fault rupture, and further contributes to geochemical variations.

Similar to the evolution of high fluid pressure, the spatial distribution of metal elements evolves from a spatially random structure to spatially clustered structures. Nine temporal sequence snapshots (Fig. 1) show the evolution and variations of geochemical patterns caused by rapid fluid pressure reductions corresponding to the later time evolution. At early time steps, cells experiencing mineral precipitation are

231 randomly observed in the system due to the random failure of one or only a few cells (Figs. 1a-1d). As the
232 system evolves, more clustered spatial distributions of geochemical patterns are produced due to the
233 occurrence of mineral precipitation among a wider range of more clustered cells (Figs. 1e-1i). The ratio of
234 nugget to sill increases before the evolutionary time of 13.6 kyr and decreases after 13.6 kyr (Fig. 2),
235 indicating that the degree of spatial dependence of geochemical patterns decreases at first and then
236 increases with the further evolution of the system. This transition might be attributed to the establishment
237 of the initial structure of incipient failures and both marks the onset of a correlation length and identifies
238 the percolation threshold of the system. Around this transition point, the number of failure events,
239 cumulative event sizes and correlation length show significant fluctuations (Miller and Nur, 2000). The
240 mineral depositional process occurs in isolated failure cells that increase the spatial randomness of the
241 geochemical patterns before the transition point. When the structure of the incipient failure is established,
242 the sub-networks at different fluid pressures merge and equilibrate according to Eq. 2; thus, a wider range
243 of fluid pressure reductions results in mineral precipitation in the form of clusters, which may enhance the
244 degree of spatial dependence of geochemical patterns.

245 A transitional phenomenon also occurs with multifractal geochemical patterns. Figure 3 shows the
246 relation between the multifractal spectrum value $f(\alpha)$ and the singularity index α for different time
247 periods. The multifractal spectrum curves vary from right deviation to left deviation at approximately 13.5
248 kyr. The increasing asymmetry index (R) with the evolution of the system demonstrates that the
249 geochemical pattern evolves from a dominant local depletion pattern to local enrichment within the entire
250 matrix near the percolation threshold. Fluid pressure reductions varying from small-scale to large-scale
251 determine the scale of superimposition of metal material at different evolutionary stages. The large-scale
252 superimposition makes the components of higher value in the whole system become more pervasively
253 distributed. Thus, the enrichment of element concentrations (asymmetry indexes R in Fig. 3) rapidly

254 increases within a short period of 1.5 kyr. The index *M* decreases with the increase of evolutionary time,
255 indicating increasingly higher degrees of multifractality (Fig. 4).

256 Simulations end when the average fluid pressure of the system reaches the failure condition. Figure 5
257 shows the corresponding final geochemical pattern, with a high degree of spatial dependence and local
258 enrichment. The highly enriched area was found to be distributed at or near the cells with high storage
259 capacity because high storage capacity equalizes the fluid pressure to a greater extent. Therefore, more
260 dramatic fluid pressure variations occur when the cells near the high storage capacity cells fail, resulting in
261 a higher magnitude of mineral depositions. This phenomenon coincides with field observations that
262 mineral deposits or veins occur at or near the faults that determine the random and clustered features of
263 ore deposits in their spatial distributions. For example, Wang et al. (2015) revealed a clustered distribution
264 of Fe deposits in space along NNE-NE trend in Fujian Province, China. The distribution of singularity
265 index α, estimated from $\log[\mu(\varepsilon_1)/\mu(\varepsilon_2)]/\log(\varepsilon_1/\varepsilon_2)$, can quantify the properties of enrichment (α<2) and
266 depletion (α>2) of geochemical elements caused by mineral depositions (Fig. 5b).

267 Producing maps of singularities can provide new information, complementing results based on the
268 original concentration distribution (Fig. 5a) and help to recognize metal concentration anomalies from
269 complex geological regions. The multifractal spectrum of the geochemical patterns is calculated via the
270 method of moments (q), and varying from -10 to 10 in steps of 1. The corresponding parameters, partition
271 function $\chi_q(\varepsilon)$, mass exponent $\tau(q)$ and singularity exponent $\alpha(q)$, are shown in Figs. 6a-6c. The
272 multifractal spectrum obtained through a Legendre transformation (Fig. 6d) shows an asymmetric left-
273 skewed shape. This asymmetry may reflect the fact that the spatial distribution of concentrations shows a
274 continuous multifractal characteristic, which can be attributed to the periodic local mineral deposition due
275 to fluid pressure fluctuation. The results shown above are based on linear relationships between solubility
276 and fluid pressure, while Figure 7 shows the simulation results with the other two relationships (Eqs. 3b
277 and 3c). These three geochemical patterns show a similar spatial structure (Figs. 7b and 7c), and both of

these spatial structures are highly dependent on the distribution of the cells' storage capacity. However, due to different solubility relationships, the accumulation of mineral precipitation varies, resulting in different degrees of local enrichment patterns at the end of the simulation as shown by the multifractal spectrum and the asymmetry index (Fig. 7d).

4. Discussion and Conclusions

We investigated the cycle of fluid pressure increase – hydrofracture – fluid pressure decrease – rapid sealing from precipitation using a cellular automaton model to simulate the singular mineralization process. With the continued increase of fluid pressure within the undrained system, the evolution of the connectivity structure shows the onset of a correlation length at the percolation threshold, after which the correlation length increases until the system as a whole reaches a critical state. The relationship between cluster size and the number of events shows a power-law with an exponential tail at the percolation threshold that plays an important role for fracture connectivity and fluid flow in the formation of mineral deposits (Roberts et al., 1998, 1999). At the critical state, the power law statistics of cluster size indicate scale invariance of the fluid pressure evolution system (cf. Fig. 6 in Miller and Nur (2000)), namely the constructed cell space can occur at the level of pore structure, or at the level of large scale fluid pressure within a fault zone. This determines that the distribution of elemental concentration also exhibits the scale-invariance property and critical thresholds where mineral phase transitions are induced by fault failure and the system seeks a new attractor (Bak et al, 1987). The scale-invariant property of geochemical patterns suggests that the snapshots in Fig. 5a can be viewed as distributions of elemental concentration at a microscopic scale (e.g. ore samples) or at a metallogenic zone scale. The non-uniform distribution of elemental concentrations on different scales occurred in nature in mineralization systems. For example, the Au concentration distribution in the Dayinggezhuang ore deposit, located in Jiaodong gold province, eastern China, suggest different mineralization density at different scales (Deng et al., 2011). Self-

organized criticality reflects complex mineralization behavior, which is characterized by a bottom-up nature where complex behavior emerges from independent but interdependent interactions of unlimited cells. For example, fluid pressure in cells far from the failure condition increases independently, however, fluid pressures in individual cells or many isolated networks will merge and equalize with each other after the structure of incipient failure is established.

The interaction of physical, chemical and biological processes can contribute to mineral deposition through phase transition or separation during the hydrothermal mineralization processes. We considered fluid pressure fluctuations and cyclicity as a dominant process in mineralization, and this cyclicity was responsible for the superposition of repeated mineralization events that ultimately produce complex geochemical patterns that can be effectively modeled using a multifractal framework. Although this idealized model is simple, it is not simplistic, and provides important insights into the singular mineralization process. Future model developments will include other important processes not yet considered, including tectonic stress increases from plate motion, to investigate how different ratios of differential stress to fluid pressure can influence the fault failure patterns which may further determine the ore deposit types (Stephens et al., 2004).

Acknowledgments

This research was jointed supported by the National Natural Science Foundation of China under Grants 41372007 and 41522206, and MOST Special Fund from the State Key Laboratory of Geological Processes and Mineral Resources, China University of Geosciences under Grant MSFGRMR25.

References

Agterberg, F. P., 1995. Multifractal modeling of the sizes and grades of giant and supergiant deposits. International Geology Review 37, 1-8.

Agterberg, F. P., 2001. Multifractal simulation of geochemical map patterns. In Geologic Modeling and Simulation (pp. 327-346). Springer, Boston, MA.

Agterberg, F. P., 2007. New applications of the model of de Wijs in regional geochemistry. Mathematical Geology 39, 1-25.

Archibald, S. M., Migdisov, A. A., Williams-Jones, A. E., 2001. The stability of Au-chloride complexes in water vapor at elevated temperatures and pressures. Geochimica et Cosmochimica Acta 65, 4413-4423.

Archibald, S. M., Migdisov, A. A., Williams-Jones, A. E., 2002. An experimental study of the stability of copper chloride complexes in water vapor at elevated temperatures and pressures. Geochimica et Cosmochimica Acta 66, 1611-1619.

Bak, P., Tang, C., Wiesenfeld, K., 1987. Self-organized criticality: An explanation of the 1/f noise. Physical review letters 59, 381-384.

Bak, P., Tang, C., 1989. Earthquakes as a self-organized critical phenomenon. Journal of Geophysical Research: Solid Earth 94, 15635-15637.

Bischoff, J. L., Rosenbauer, R. J., Pitzer, K. S., 1986. The system NaCl-H2O: Relations of vapor-liquid near the critical temperature of water and of vapor-liquid-halite from 300 to 500 C. Geochimica et Cosmochimica Acta 50, 1437-1444.

Bischoff, J. L., Rosenbauer, R. J., 1988. Liquid-vapor relations in the critical region of the system NaCl-H2O from 380 to 415 C: A refined determination of the critical point and two-phase boundary of seawater. Geochimica et Cosmochimica Acta 52, 2121-2126.

Blanpied, M. L., Lockner, D. A., Byerlee, J. D., 1992. An earthquake mechanism based on rapid sealing of faults. Nature 358, 574.

348 Bodnar, R. J., Cannatelli, C., De Vivo, B., Lima, A., Belkin, H. E., Milia, A., 2007. Quantitative model for
349 magma degassing and ground deformation (bradyseism) at Campi Flegrei, Italy: Implications for
350 future eruptions. Geology 35, 791-794.
351 Cambardella, C. A., Moorman, T. B., Parkin, T. B., Karlen, D. L., Novak, J. M., Turco, R. F., Konopka, A. E.,
352 1994. Field-scale variability of soil properties in central Iowa soils. Soil science society of America
353 Journal 58, 1501-1511.
354 Cheng, Q., Agterberg, F. P., Ballantyne, S. B., 1994. The separation of geochemical anomalies from
355 background by fractal methods. Journal of Geochemical Exploration 51, 109-130.
356 Cheng, Q., Agterberg, F. P., 1996. Multifractal modeling and spatial statistics. Mathematical Geology 28, 1-
357 16.
358 Cheng, Q., 1999. Multifractality and spatial statistics. Computers & Geosciences 25, 949-961.
359 Cheng, Q., Xu, Y., Grunsky, E., 2000. Integrated spatial and spectrum method for geochemical anomaly
360 separation. Natural Resources Research 9, 43-52.
361 Cheng, Q., 2005. Multifractal distribution of eigenvalues and eigenvectors from 2D multiplicative cascade
362 multifractal fields. Mathematical Geology 37, 915-927.
363 Cheng, Q., 2007. Mapping singularities with stream sediment geochemical data for prediction of
364 undiscovered mineral deposits in Gejiu, Yunnan Province, China. Ore Geology Reviews 32, 314-324.
365 Cheng, Q., 2008. Non-linear theory and power-law models for information integration and mineral
366 resources quantitative assessments. Mathematical Geosciences 40, 503-532.
367 Cheng, Q., 2014. Generalized binomial multiplicative cascade processes and asymmetrical multifractal
368 distributions. Nonlinear Processes in Geophysics 21, 477-487.
369 Cox, S. F., 1995. Faulting processes at high fluid pressures: an example of fault valve behavior from the
370 Wattle Gully Fault, Victoria, Australia. Journal of Geophysical Research: Solid Earth 100, 12841-12859.

David, C., Wong, T. F., Zhu, W., Zhang, J., 1994. Laboratory measurement of compaction-induced permeability change in porous rocks: Implications for the generation and maintenance of pore pressure excess in the crust. Pure and Applied Geophysics 143, 425-456.

Deng, J., Wang, Q., Wan, L., Liu, H., Yang, L., Zhang, J., 2011. A multifractal analysis of mineralization characteristics of the Dayingezhuang disseminated-veinlet gold deposit in the Jiaodong gold province of China. Ore Geology Reviews 40, 54-64.

De Wijs, H., 1951. Statistics of ore distribution. Part I: frequency distribution of assay values. Journal of the Royal Netherlands Geological and Mining Society 13, 365-375.

Evertsz, C. J. G., Mandelbrot, B. B., 1992, Multifractal measures (Appendix B) [A], in Peitgen,H.-O., Jurgens, H., and Saupe, D., eds., Chaos and fractals [C]: Springer Verlag, New York,p. 922–953.

Fitzenz, D. D., Miller, S. A., 2001. A forward model for earthquake generation on interacting faults including tectonics, fluids, and stress transfer. Journal of Geophysical Research: Solid Earth 106, 26689-26706.

Goovaerts, P., 1999. Geostatistics in soil science: state-of-the-art and perspectives. Geoderma 89, 1-45.

Halsey, T. C., Jensen, M. H., Kadanoff, L. P., Procaccia, I., Shraiman, B. I., 1986. Fractal measures and their singularities: The characterization of strange sets. Physical Review A 33, 1141.

Helgeson, H. C., Lichtner, P. C., 1987. Fluid flow and mineral reactions at high temperatures and pressures. Journal of the Geological Society 144, 313-326.

Ko, S. C., Olgaard, D. L., Briegel, U., 1995. The transition from weakening to strengthening in dehydrating gypsum: Evolution of excess pore pressures. Geophysical Research Letters 22, 1009-1012.

Loucks, R. R., Mavrogenes, J. A., 1999. Gold solubility in supercritical hydrothermal brines measured in synthetic fluid inclusions. Science 284, 2159-2163.

Mandelbrot, B. B., 1983. The fractal geometry of nature (Vol. 173, p. 51). New York: WH freeman.

Matheron, G., 1962. Traité de géostatistique appliquée. 1 (1962) (Vol. 1). Editions Technip.

Migdisov, A. A., Williams-Jones, A. E., Suleimenov, O. M., 1999. Solubility of chlorargyrite (AgCl) in water vapor at elevated temperatures and pressures. Geochimica et Cosmochimica Acta 63, 3817-3827.

Migdisov, A. A., Williams-Jones, A. E., 2005. An experimental study of cassiterite solubility in HCl-bearing water vapour at temperatures up to 350 C. Implications for tin ore formation. Chemical geology 217, 29-40.

Migdisov, A. A., Williams-Jones, A. E., 2013. A predictive model for metal transport of silver chloride by aqueous vapor in ore-forming magmatic-hydrothermal systems. Geochimica et Cosmochimica Acta 104, 123-135.

Migdisov, A. A., Bychkov, A. Y., Williams-Jones, A. E., Van Hinsberg, V. J., 2014. A predictive model for the transport of copper by HCl-bearing water vapour in ore-forming magmatic-hydrothermal systems: Implications for copper porphyry ore formation. Geochimica et Cosmochimica Acta 129, 33-53.

Miller, S. A., Nur, A., Olgaard, D. L., 1996. Earthquakes as a coupled shear stress-high pore pressure dynamical system. Geophysical Research Letters 23, 197-200.

Miller, S. A., Ben ‐ Zion, Y., Burg, J. P., 1999. A three ‐ dimensional fluid ‐ controlled earthquake model: Behavior and implications. Journal of Geophysical Research: Solid Earth 104, 10621-10638.

Miller, S. A., Nur, A., 2000. Permeability as a toggle switch in fluid-controlled crustal processes. Earth and Planetary Science Letters 183, 133-146.

Miller, S. A., 2002. Properties of large ruptures and the dynamical influence of fluids on earthquakes and faulting. Journal of Geophysical Research: Solid Earth 107.

Miller, S. A., Van Der Zee, W., Olgaard, D. L., Connolly, J. A. D., 2003. A fluid-pressure feedback model of dehydration reactions: experiments, modelling, and application to subduction zones. Tectonophysics 370, 241-251.

417 Moncada, D., Rimstidt, J. D., Bodnar, R. J., 2019. How to form a giant epithermal precious metal deposit:
418 Relationships between fluid flow rate, metal concentration of ore-forming fluids, duration of the ore-
419 forming process, and ore grade and tonnage. Ore Geology Reviews 113, 103066.
420 Peterson, E. C., Mavrogenes, J. A., 2014. Linking high-grade gold mineralization to earthquake-induced
421 fault-valve processes in the Porgera gold deposit, Papua New Guinea. Geology 42, 383-386.
422 Rempel, K. U., Migdisov, A. A., & Williams-Jones, A. E., 2006. The solubility and speciation of
423 molybdenum in water vapour at elevated temperatures and pressures: Implications for ore genesis.
424 Geochimica et Cosmochimica Acta 70, 687-696.
425 Rice, J. R., 1992. Fault stress states, pore pressure distributions, and the weakness of the San Andreas fault.
426 In International geophysics 51, 475-503.
427 Roberts, S., Sanderson, D. J., Gumiel, P., 1998. Fractal analysis of Sn-W mineralization from central Iberia;
428 insights into the role of fracture connectivity in the formation of an ore deposit. Economic Geology 93,
429 360-365.
430 Roberts, S., Sanderson, D. J., Gumiel, P., 1999. Fractal analysis and percolation properties of veins.
431 Geological Society, London, Special Publications 155, 7-16.
432 Sanchez-Alfaro, P., Reich, M., Driesner, T., Cembrano, J., Arancibia, G., Pérez-Flores, P., Heinrich, C.A.,
433 Rowland, J., Tardani, D., Lange, D., Campos, E., 2016. The optimal windows for seismically-enhanced
434 gold precipitation in the epithermal environment. Ore Geology Reviews 79, 463-473.
435 Schertzer, D., Lovejoy, S., 1987. Physical modeling and analysis of rain and clouds by anisotropic scaling
436 multiplicative processes. Journal of Geophysical Research: Atmospheres 92, 9693-9714.
437 Segall, P., Rice, J. R., 1995. Dilatancy, compaction, and slip instability of a fluid‐infiltrated fault. Journal of
438 Geophysical Research: Solid Earth 100, 22155-22171.
439 Seward, T. M., 1973. Thio complexes of gold and the transport of gold in hydrothermal ore solutions.
440 Geochimica et Cosmochimica Acta 37, 379-399.

441 Sibson, R. H., 1987. Earthquake rupturing as a mineralizing agent in hydrothermal systems. Geology 15(8),
442 701-704.
443 Sibson, R. H., Robert, F., Poulsen, K. H., 1988. High-angle reverse faults, fluid-pressure cycling, and
444 mesothermal gold-quartz deposits. Geology 16, 551-555.
445 Sibson, R. H., 1992. Implications of fault-valve behaviour for rupture nucleation and recurrence.
446 Tectonophysics 211, 283-293.
447 Sleep, N. H., Blanpied, M. L., 1992. Creep, compaction and the weak rheology of major faults. Nature 359,
448 687.
449 Sprunt, E. S., Nur, A., 1977. Destruction of porosity through pressure solution. Geophysics 42, 726-741.
450 Stephens, J. R., Mair, J. L., Oliver, N. H., Hart, C. J., Baker, T., 2004. Structural and mechanical controls on
451 intrusion-related deposits of the Tombstone Gold Belt, Yukon, Canada, with comparisons to other
452 vein-hosted ore-deposit types. Journal of Structural Geology 26, 1025-1041.
453 Wang, Z., Zuo, R., Zhang, Z., 2015. Spatial analysis of Fe deposits in Fujian Province, China: Implications
454 for mineral exploration. Journal of Earth Science 26, 813-820.
455 Walder, J., Nur, A., 1984. Porosity reduction and crustal pore pressure development. Journal of
456 Geophysical Research: Solid Earth 89, 11539-11548.
457 Walther, J. V., Helgeson, H. C., 1977. Calculation of the thermodynamic properties of aqueous silica and
458 the solubility of quartz and its polymorphs at high pressures and temperatures. American Journal of
459 Science 277, 1315-1351.
460 Weatherley, D. K., Henley, R. W., 2013. Flash vaporization during earthquakes evidenced by gold deposits.
461 Nature Geoscience 6, 294-298.
462 Wilkinson, J. J., Johnston, J. D., 1996. Pressure fluctuations, phase separation, and gold precipitation during
463 seismic fracture propagation. Geology 24, 395-398.
464 Wolfram, S., 1984. Cellular automata as models of complexity. Nature 311, 419-424.

Wong, T. F., Ko, S. C., Olgaard, D. L., 1997. Generation and maintenance of pore pressure excess in a dehydrating system 2. Theoretical analysis. Journal of Geophysical Research: Solid Earth 102, 841-852.

Xie, S., Bao, Z., 2004. Fractal and multifractal properties of geochemical fields. Mathematical Geology 36, 847-864.

Zuo, R., Cheng, Q., Agterberg, F. P., Xia, Q., 2009. Application of singularity mapping technique to identify local anomalies using stream sediment geochemical data, a case study from Gangdese, Tibet, western China. Journal of Geochemical Exploration 101, 225-235.

Zuo, R., Wang, J., 2016. Fractal/multifractal modeling of geochemical data: A review. Journal of Geochemical Exploration 164, 33-41.

Zuo, R., 2016. A nonlinear controlling function of geological features on magmatic-hydrothermal mineralization. Scientific Reports 6, 27127.

Zuo, R., 2018. A fractal measure of mass transfer in fluid–rock interaction. Ore Geology Reviews 95, 569–574.

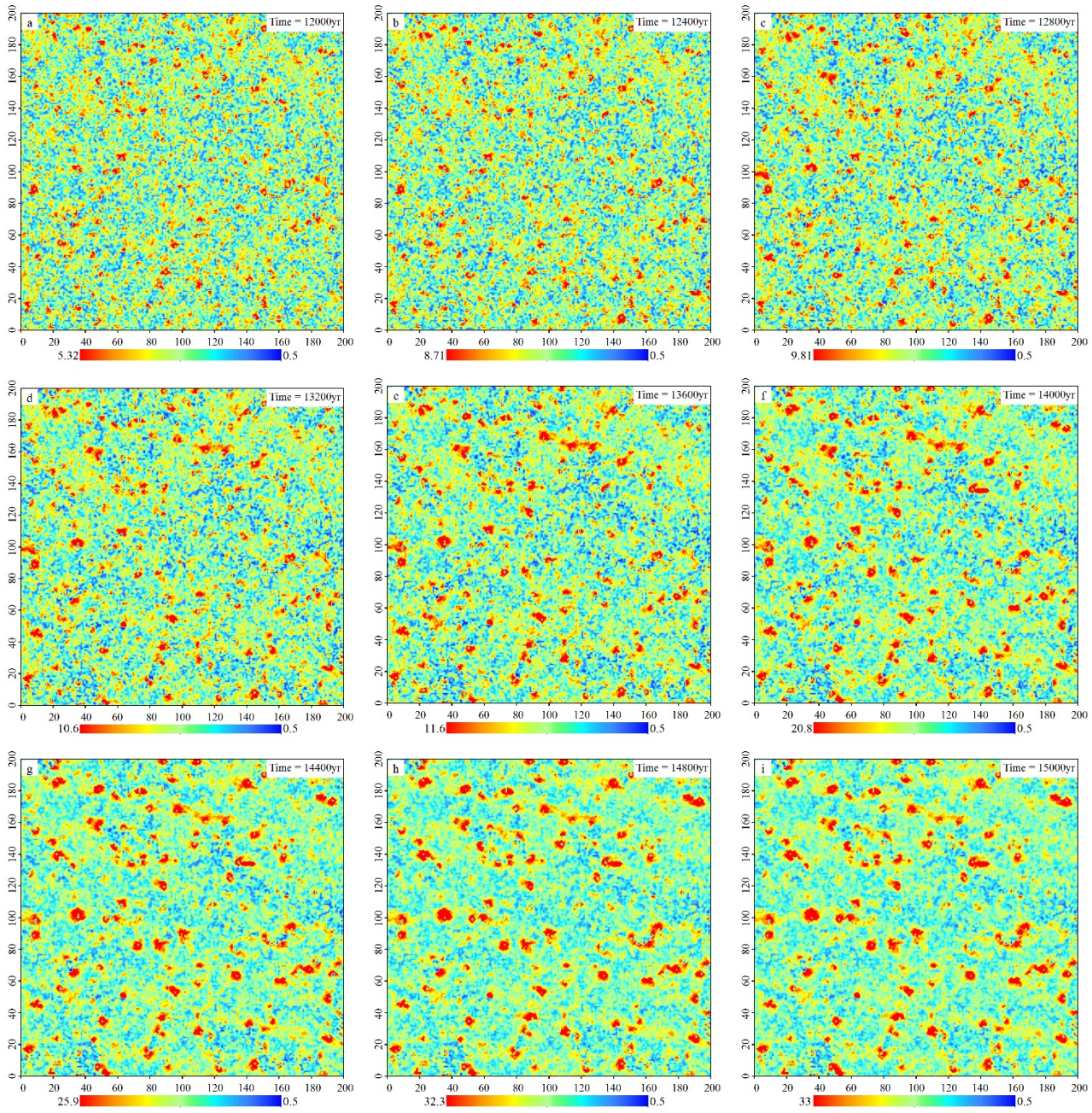

Figure 1. Nine temporal sequence snapshots showing the evolution and variations of geochemical patterns caused by rapid fluid pressure reductions corresponding to time of evolution; At early times, from (a) to (d), cells with mineral deposition randomly occur in the system due to the random failure of one or only a few cells. As the system evolves, from (e) to (i), structured spatial distributions of geochemical patterns are produced due to the occurrence of mineral deposition among a wider range of clustered cells.

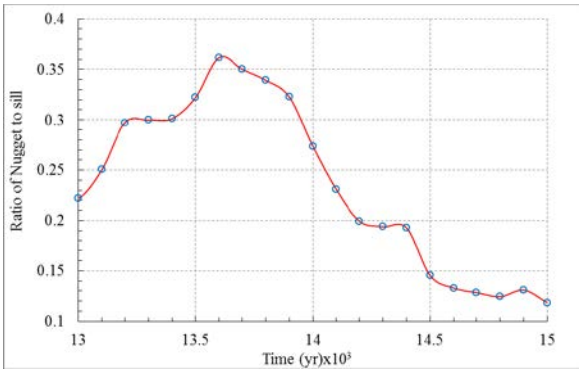

Figure 2. Time line of ratio of nugget to sill obtained from the semivariogram function.

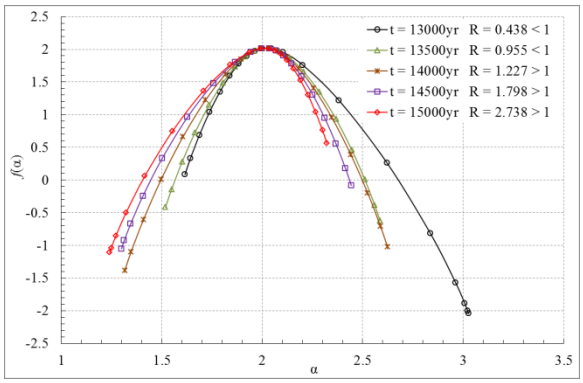

498

499 Figure 3. Multifractal spectra of geochemical patterns at different evolution times.

500

501

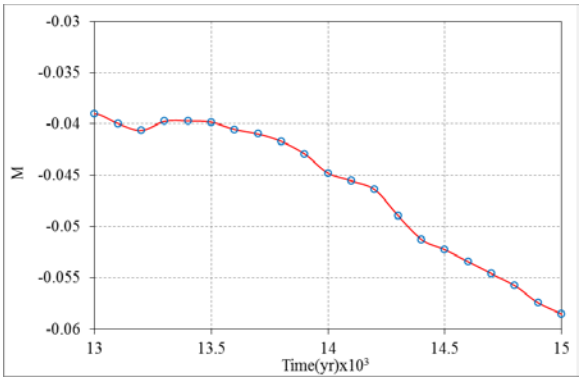

502 Figure 4. Time line of multifractality measuring the irregularity of geochemical spatial dispersion patterns.

503

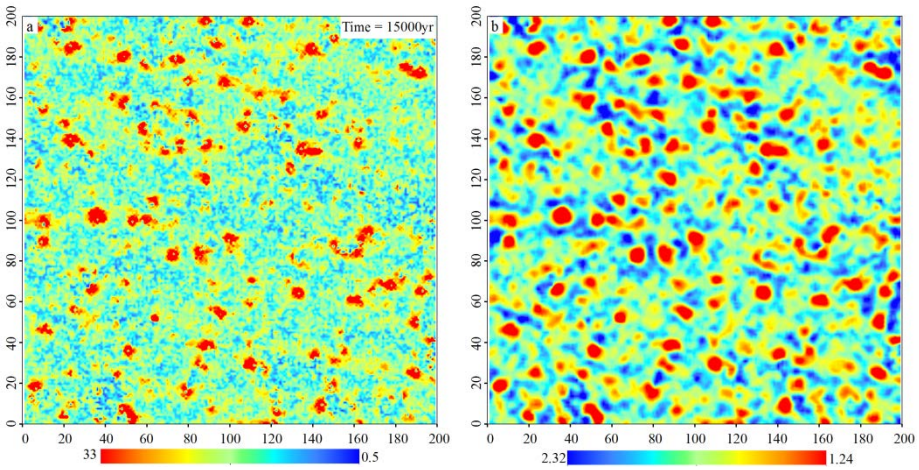

Figure 5. (a) Spatial distribution of element concentration based on linear relationships between solubility and pressure; (b) Spatial distribution of singularity index α quantifying the properties of local enrichment and depletion of geochemical patterns.

509

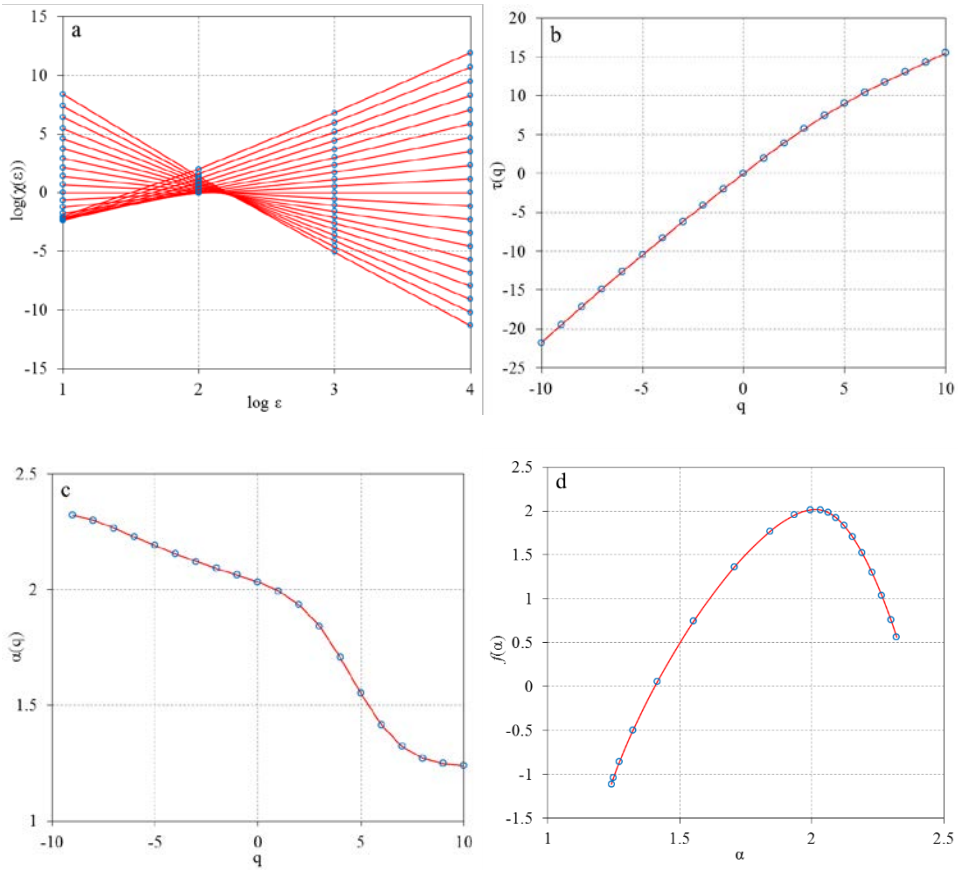

510

511

512 Figure 6. Results of multifractal analysis applied to geochemical pattern of Figure 5(a); (a) Log-log plot of
513 mass-partition function vs. edge size of cell, model parameter q varies from -10 to 10 with 1 interval; (b)
514 Estimates of mass exponent $\tau(q)$ involve slopes of the straight-lines in (a) vs. order q; (c) Singularity index
515 $\alpha(q)$ and order q; (d) Multifractal spectra value $f(\alpha)$ vs singularity index α .

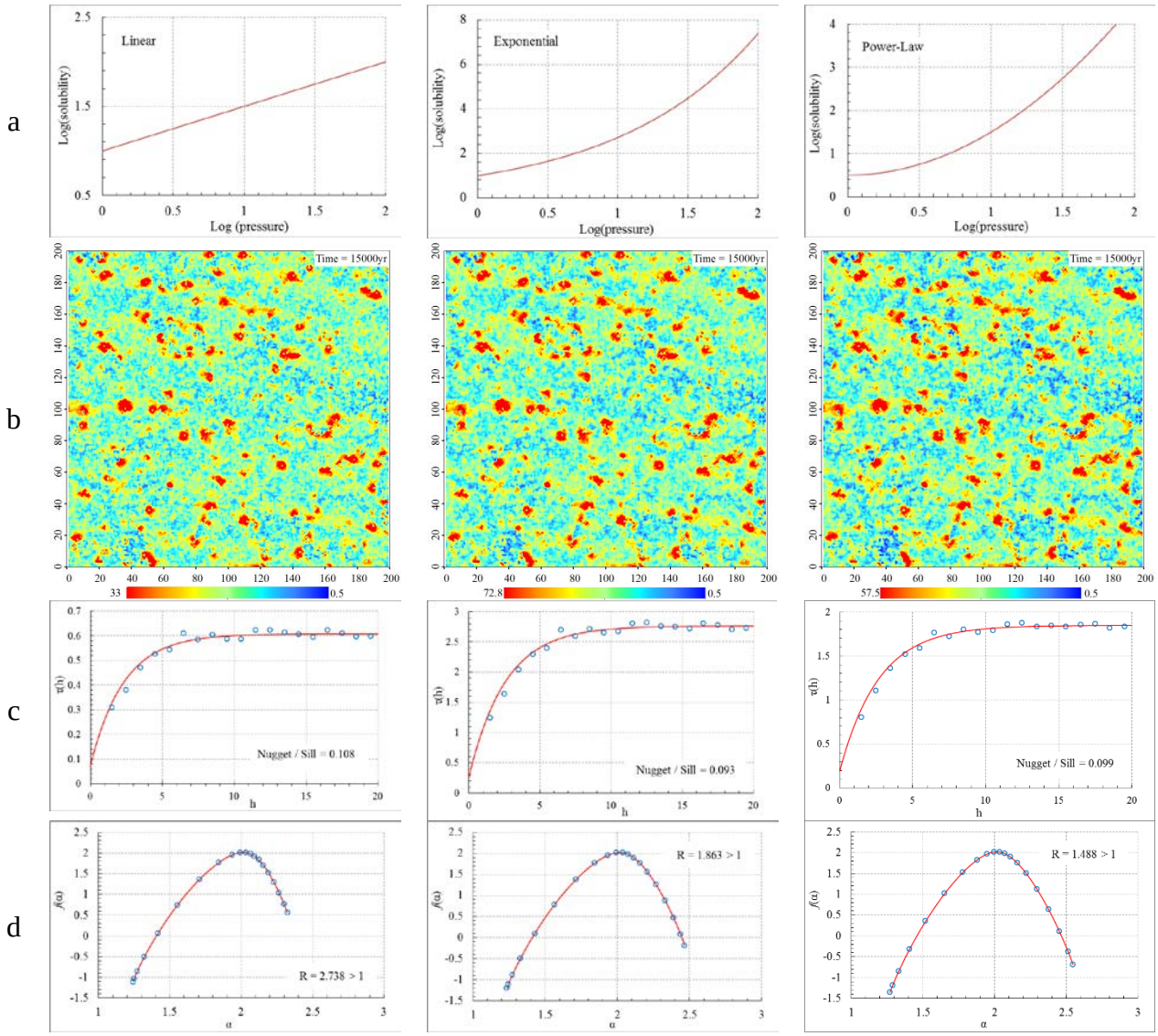

Figure 7. Row (a) Three different relationships (linear, exponential and power law) between solubility and pressure in logarithmic coordinates; Row (b) Spatial distribution of element concentration based on three different relationships based on Row (a); Row (c) and Row (d) are semivariograms and multifractal spectrums corresponding to geochemical patterns in Row (b).